Biosensors and Bioelectronics 133 (2019) 55–63

Contents lists available at ScienceDirect

Biosensors and Bioelectronics

journal homepage: www.elsevier.com/locate/bios

$NiCo_2O_4$ spinel embedded with carbon nanotubes derived from bimetallic NiCo metal-organic framework for the ultrasensitive detection of human immune deficiency virus-1 gene

Zhankui Jia[a], Yashen Ma[b], Longyu Yang[b], Chuanpan Guo[b], Nan Zhou[a,*], Minghua Wang[a,b], Linghao He[b], Zhihong Zhang[b,*]

[a] The First Affiliated Hospital of Zhengzhou University, No. 1, Jianshe East Road, Zhengzhou 450052, PR China
[b] Henan Provincial Key Laboratory of Surface and Interface Science, Zhengzhou University of Light Industry, No. 136, Science Avenue, Zhengzhou 450001, PR China

ARTICLE INFO

Keywords:
Electrochemical biosensor
Bimetallic metal-organic framework
Detection of HIV-1
Nickel/cobalt oxide spinel
Calcination of MOFs

ABSTRACT

A bimetallic NiCo-based metal-organic framework (NiCo-MOF) was pyrolyzed into a novel composite comprising $NiCo_2O_4$ spinel, CoO, and metallic Co/Ni nanoparticles embedded with carbon nanotubes at high temperature 700 °C under N_2 atmosphere (represented by $NiCo_2O_4$/CoO@CNTs), whereas organic ligands were almost decomposed in H_2 atmosphere, leading to absence of carbon nanotubes (denoted by $NiCo_2O_4$/CoO). The feasibility of using the composite as efficient bioplatform for immobilizing the probe DNA of human immune deficiency virus-1 (HIV-1) in the electrochemical detection of the HIV-1 DNA was explored. Compared with the pristine NiCo-MOF and $NiCo_2O_4$/CoO, the $NiCo_2O_4$/CoO@CNTs composite exhibited high electrochemical activity, good biocompatibility, and strong bioaffinity toward the probe DNA. Electrochemical measurements demonstrated that the $NiCo_2O_4$/CoO@CNTs-based bioassay displayed superior sensing performances, giving an ultralow detection limit of 16.7 fM toward HIV-1 DNA over the linear range of 0.1 pM to 20 nM; possessing high selectivity even against noncomplementary and two-base mismatch sequences; exhibiting good stability, reproducibility, repeatability and applicability in the application of detecting human serum samples. Thus, the present strategy can broaden the application of MOFs and their derivatives in various fields of biosensing.

1. Introduction

The early detection of HIV biomarkers or genes is crucial for the diagnosis, treatment, and hampering the propagation of AIDS (Ambinder et al., 2010). However, current diagnostic methods for AIDS, including the detection of HIV antibody and/or HIV antigen, are difficult to fulfill this urgent requirement due to relatively long time of HIV antibody production (weeks to months). And in this period, the amounts of HIV antibodies will be too insufficient to be detected. Thus, more immunoassay-based nucleic acid detections have been proved to the efficacious approaches for the early detection of HIV-1 (Zhao et al., 2015). And conventional gene detection assays are based on the hybridization between DNA or RNA probes and related complementary HIV-1 genes (Qaddare and Salimi, 2017). Although numerous efforts have focused on the fabrication of biosensors for HIV-1 gene detection, the majority of reported DNA biosensor arrays are founded on optical transduction principles, such as fluorescence (Lillis et al., 2016), Raman scattering (Otange et al., 2017), and chemiluminescence (Ali et al., 2017). DNA biosensor arrays based on optical readout exhibit various advantages, such as high sensitivity and throughput (hundreds of thousands of probes), but require expensive instrument for optical imaging, laser light, and labeled probes. Therefore, it is extremely urgent to develop more analytical and diagnostic techniques which can detect HIV more early, accurately, sensitively and specifically.

Electrochemical biosensors have drawn more and more attention due to their compelling advantages, such as facile fabrication, rapid detection, good selectivity and sensitivity (Rackus et al., 2015). DNA sensors can detect a specific DNA fragment on the basis of hybridization with a complementary DNA fragment. Electrochemical gene sensors for the ultratrace and label-free determination of DNA hybridization for HIV-1 gene detection with ultrahigh sensitivity, specific selectivity, and rapid analysis can be developed by using a variety of nanomaterials, such as EuS nanoclusters (Babamiri et al., 2018), CD4(+) T lymphocytes (Carinelli et al., 2015), and P-RGO@Au@Ru-SiO_2 (Zhou et al., 2015). Given that the sensitivity of electrochemical biosensors could be improved via the integration of nanomaterials with excellent electrical

---

* Corresponding authors.
E-mail address: fcczhoun@zzu.edu.cn (N. Zhou).

https://doi.org/10.1016/j.bios.2019.03.030
Received 28 January 2019; Received in revised form 12 March 2019; Accepted 17 March 2019

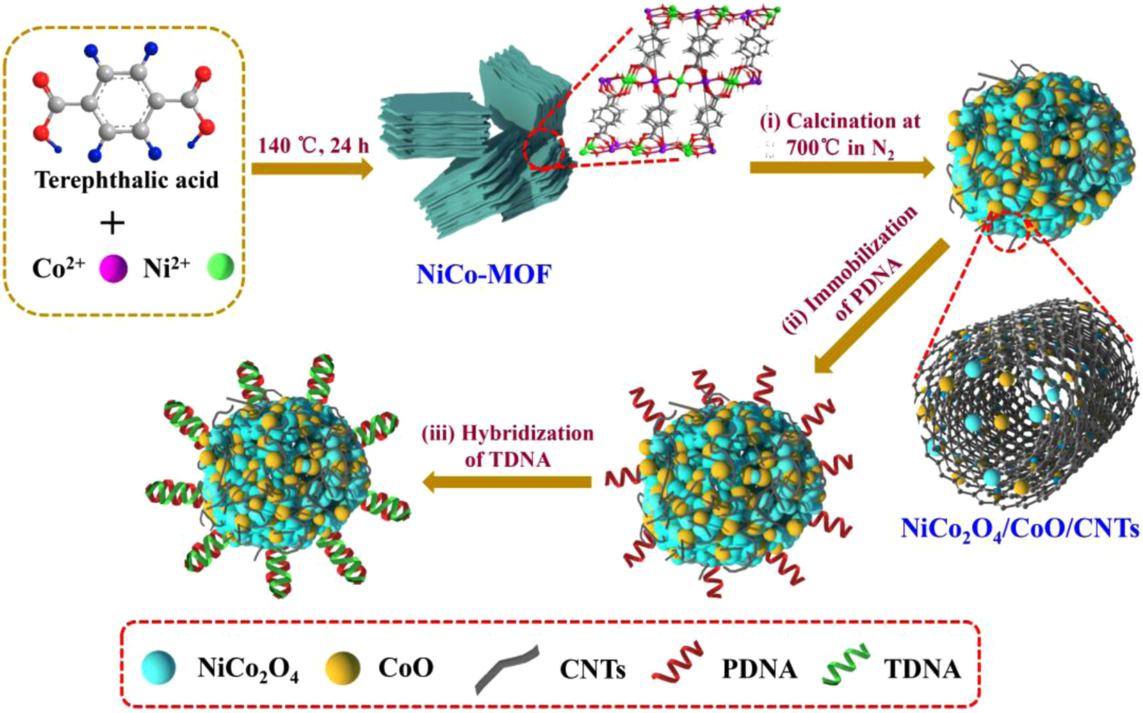

Scheme 1. Schematic diagram of the fabrication procedure of the $NiCo_2O_4$/CoO/CNTs-based assay for detecting HIV-1 DNA, including (i) the fabrication of the $NiCo_2O_4$/CoO/CNTs-based assay, (ii) the immobilization of the probe DNA, and (iii) the detection of the HIV-1 DNA.

and large surface areas during electrode surface configuration, the selection of electrode materials with large specific surface areas, excellent electrochemical activity, strong bioaffinity with biomolecules, good biocompatibility, and outstanding stability in aqueous solutions is highly critical.

Metal-organic frameworks (MOFs) are composed of metal ions or clusters linked by organic ligands and have demonstrated promising sensing applications. They have been used as chemical sensors, gas sensors, biosensors, and fluorescence sensors due to their attractive properties of large surface areas, tunable porosities, organic functionalities, stable shelf lives, and excellent thermal stabilities (Zhu and Xu, 2014). The organic linkers involved in MOFs possess a conjugated π-electron system and offer a source of potential hydrogen bonds that enable appropriate interactions between MOFs and single-stranded DNA. MOFs can recognize DNA or other biomolecules via electrochemical signal changes. These characteristics further broaden the applications of MOFs in the early diagnosis of cancers or diseases. The series of Zr-MOFs, Al-MOF, Fe-MOF, and Zn-MOF were employed as the bioplatforms for detecting different cancer markers or other analytes (Guo et al., 2017; He et al., 2017; Zhang et al., 2017; Zhou et al., 2019). Nevertheless, most MOFs have limited practical applications in electrochemical biosensors due to the low electrochemical activity and poor stability (Du et al., 2014). Currently, MOF-related biosensors for HIV-1 gene detection are mainly based on fluorescence emission spectroscopy (Chen et al., 2013; Pan et al., 2018). Recently, MOFs are suitable precursors for the in situ synthesis of well-dispersed metal nanoparticles (NPs) wrapped in porous graphitic carbon layers via pyrolysis under an inert atmosphere, which can partially preserve the unique morphology, high porosity, large surface area, and well-dispersed functional elements of the NPs. Graphitic carbon generated in situ also has high electron mobility and extended π-π conjugation structure (Wang et al., 2011). It can simultaneously boost charge separation/electron transfer and intensively bind with DNA strands, which would improve detection sensitivity toward analytes. Therefore, complexes of metal oxides and graphitic carbon can overcome the disadvantages presented by pristine MOFs when employed as electrochemical biosensor scaffolds. The utilization of MOFs as templates in the synthesis of metal oxide/carbon nanocomposites is a facile and efficient method for improving the electrochemical performance of MOFs (Liu et al., 2014). High-performance nonenzymatic glucose and H_2O_2 electrochemical sensors have been fabricated by immobilizing NiMOF/Ni/NiO/C nanocomposites derived from Ni-MOF onto glassy carbon electrodes with Nafion film (Shu et al., 2017). A CeO_{2-x}/C/rGO nanocomposite derived from Ce-MOF has been developed and utilized for uric acid detection (Peng et al., 2018). The derivative obtained from the bimetallic cerium/copper-based MOF by the pyrolysis at different temperatures was explored as the scaffold of electrochemical aptamer sensors for extremely sensitive detection of trace tobramycin (Wang et al., 2019).

As one kind of electrochemically active metals, Co/Ni-related MOFs or there derivatives were widely explored as catalysts for clean energy conversion, energy transfer, or biosensing (Jin et al., 2019; Li et al., 2019; Rezaee and Shahrokhian, 2019). However, most of them were applied as catalysts, not as platforms of DNA biosensors. Additionally, because the type of atmosphere plays an important role in the formation of the MOF-derived nanocomposites in the calcination procedure (Zhong et al., 2017a). Although there are some reports on the MOFs derivatives as the biosensor platforms (Wang et al., 2018b; Zhang et al., 2017), the systematic investigation on the effect of the atmosphere used in pyrolysis on the components of the formed nanocomposites and biosensing performances were seldom investigated. Additionally, to the best of our knowledge, studies on the applications of the complexes of metal oxides and mesoporous carbon derived from MOFs as electrochemical biosensors for HIV-1 gene determination have not been reported yet.

In this work, we produced novel composites of $NiCo_2O_4$, CoO, and metallic Co/Ni oxide by synthesizing and subjecting bimetallic NiCo-MOF to high-temperature treatment under N_2 and H_2 atmospheres. Subsequently, the derivatives from NiCO-MOF was explored as the platforms for the HIV-1 probe DNA immobilization and detection of the HIV-1 targete DNA (Scheme 1). Herein, two kinds of atmospheres, H_2 and N_2, were applied in the pyrolysis of NiCo-MOF nanosheets at high temperature. Different nanostructures and chemical components of the derivatives were obtained, which further affected the immobilization behavior of the probe DNA and detection of the target HIV-1 DNA. Therefore, it is believed that this optimized NiCo-MOF-derivative is also one kind of promising candidates for multifunctional applications in biosensors. As compared with the pristine NiCo-MOF and the derivative from NiCo-MOF calcined under H_2 atmosphere, the results demonstrated that the nanocomposite obtained from NiCo-MOF calcined under N_2 atmosphere exhibited the superior sensing performance for the HIV-1 DNA detection. This work can extend the application of MOFs and their derivatives in early diagnosis of diseases.

2. Experimental section

The parts of materials and regents, preparation of all solutions, pretreatment of the bare Au electrode (AE), and basic characterizations, were supplied in the S1 section (See the Supplementary material). Moreover, a nonlinear least-squares method was applied to fit and determine the parameters of the electron-elements in an equivalent circuit (Fig. S1).

2.1. Synthesis of NiCo-MOF, $NiCo_2O_4$/CoO, and $NiCo_2O_4$/CoO/CNTs composites

According to the reported literature (Wu et al., 2019), the NiCo-MOF was prepared by a modified approach. In brief, $CoCl_2·6H_2O$ (0.375 mmol), 0.375 mmol $NiCl_2·6H_2O$, and 0.75 mmol terephthalic acid are added to 36 mL solution (32 mL of N, N-dimethylformamide, 2 mL of ethanol and 2 mL of Milli-Q H_2O) for ultrasonic uniformity. The resultant mixture was transferred into to a Teflon-lined stainless steel autoclave (45 mL), following by keeping static at 140 °C temperature for 24 h. Afterward, it was washed centrifugally with Milli-Q water and dried under vacuum at 60 °C for 6 h.

In typical, the NiCo-MOF wan calcined in a tube furnace under flow H_2 and N_2 atmospheres with the heating rate of 2 °C min^{-1} until the temperature was up to 700 °C respectively. Afterward, the calcination system was remained at 700 °C for additional 2 h. According to the chemical components of the obtained nanocomposites, the final products were represented as $NiCo_2O_4$/CoO and $NiCo_2O_4$/CoO/CNTs under flow H_2 and N_2 atmospheres, respectively.

2.2. Fabrication of the NiCo-MOF-, $NiCo_2O_4$/CoO-, and $NiCo_2O_4$/CoO/CNTs-based DNA sensors

Taking the fabrication of the $NiCo_2O_4$/CoO/CNTs-based assay as an example, the preparation procedure was performed as follows: the $NiCo_2O_4$/CoO/CNTs composite (1.0 mg) was dispersed in 1.0 mL of Milli-Q water and ultrasonic agitated for 30 min until the formation of a homogeneous suspension, giving a concentration of 1.0 mg mL^{-1}. Afterward, the homogeneous $NiCo_2O_4$/CoO/CNTs suspension (5.0 µL) was dropped into the cleaned AE surface and dried in ambient air for 12 h. Thus, the modified electrode was denoted as $NiCo_2O_4$/CoO/CNTs/AE. Afterward, the $NiCo_2O_4$/CoO/CNTs was immersed into the probe DNA solution (100 nM) for 30 min and washed with phosphate buffered solution (PBS, 0.01 M, pH 7.4) thoroughly to remove the physically adsorbed DNA strands. The obtained electrochemical assay was labeled as PDNA/$NiCo_2O_4$/CoO/CNTs/AE. When detecting the complementary HIV target DNA, the obtained was marked as TDNA/PDNA/$NiCo_2O_4$/CoO/CNTs/AE. For comparison, the preparation procedures of NiCo-MOF and $NiCo_2O_4$/CoO suspensions and their corresponding assays were also prepared in the same manner. As such, the resultant suspensions for different nanomaterials were further used to develop various DNA assays to detect HIV gene. Additionally, to assess the selectivity of the as-developed DNA assay, non-complementary DNA and two-base mismatch DNA solutions were used.

2.3. Electrochemical measurements

Electrochemical measurements were performed on CHI760E electrochemical workstation (Chenhua, Shanghai, China). It was equipped with a common three-electrode system, which is composed of the counter electrode (Pt wire), the reference electrode (Ag/AgCl with saturated KCl) and the working electrode (an Au electrode or modified Au electrode). Cyclic voltammetry (CV) measurements were investigated within a potential range from − 0.2–0.8 V at the scan rate of 50 mV s^{-1} in 0.01 M PBS solution (pH 7.4) containing 0.1 KCl, 5 mM $K_3[Fe(CN)_6]$, and 5 mM $K_4[Fe(CN)_6]$. Electrochemical impedance spectroscopy (EIS) measurements were performed within the frequency range of 0.01 Hz–100 kHz with amplitude of 5 mV under open circuit potential. All EIS data were simulated using the Zview2 software. The simulated equivalent circuit is consisted of solution resistance (R_s), charge-transfer resistance (R_{ct}), constant-phase element (CPE), and Warburg impedance (W_o) (the inset in Fig. S1). In the present work, each electrochemical measurement was repeated at least three times and also conducted at least in triplicate with different electrodes to ensure the accuracy of the experimental data.

3. Results and discussion

3.1. Surface morphologies of NiCo-MOF, $NiCo_2O_4$/CoO, and $NiCo_2O_4$/CoO/CNTs composites

The surface morphologies and structural characteristics of the NiCo-MOF, $NiCo_2O_4$/CoO, and $NiCo_2O_4$/CoO/CNTs were determined through Field emission scanning electron microscope (FE-SEM) and transmission electron microscopy (TEM). The SEM and TEM images of the materials are presented in Figs. S2, S3, and 1. The surface morphology of the NiCo-MOF revealed the presence of stacked ultrathin sheets (Figs. S2a and S2b), which were also observed in TEM images (Fig. S2c). As reported in the referred literature (Zhao et al., 2016), Co and Ni atoms are octahedrally coordinated by six O atoms, and these pseudo octahedra are further edge/corner connected with each other along the [010]/[001] direction in the (200) crystallographic plane to form 2D bimetal layers separated by terephthalic acid molecules. The majority of NPs were embedded within the nanosheets, as shown through high-resolution TEM (HR-TEM) imaging (Fig. S2e). A clear fringe with an interplanar spacing of 0.22 nm that corresponded to the (200) planes of the CoO nanoparticles was observed (Huo et al., 2014). NPs in the derivatives accumulated within pores after calcination at 700 °C under H_2 and N_2 atmospheres (Fig. S3). The TEM images of $NiCo_2O_4$/CoO and $NiCo_2O_4$/CoO/CNTs are shown in Fig. 1. The TEM image of the $NiCo_2O_4$/CoO composite (Figs. 1**a** and 1**b**) shows the presence of large aggregated NPs that were composed of original nanosheets (Figs. 1**b** and 1**c**). The derivative obtained through the calcination of NiCo-MOF under N_2 atmosphere exhibited small NPs that were surrounded by nanotubes. The HR-TEM images of $NiCo_2O_4$/CoO and $NiCo_2O_4$/CoO/CNTs were acquired to further probe the microstructure of the nanocomposites, as illustrated in Figs. 1**c** and 1**f**. Lattice fringes with interplanar spacings of 0.24 nm corresponded to the (311) planes of $NiCo_2O_4$ (JCPDS No. 73–1702), whereas those with spacing of 0.22 nm was attributed to the (200) plane of CoO. These results hint that the derivatives of NiCo-MOF calcined under different atmospheres at high temperature showed different nanostructures. The metal coordination centers changed to $NiCo_2O_4$ and CoO nanoparticles, while the organic ligands were transferred to CNTs under N_2 atmosphere but were fully decomposed under H_2 atmosphere. The similar observation was obtained by Zhong et al., of which Co NPs embedded N-doped CNTs derived from calcination of MOF precursor under N_2 atmosphere at 700–900 °C (Zhong et al., 2017b). However, Aijaz A et al. reported a method for the synthesis of core-shell spinel Co oxide nanoparticles (Co@Co_3O_4) encapsulated in in situ formed N-doped carbon nanotube (CNT)-grafted carbon polyhedra by carbonization of N-containing MOF

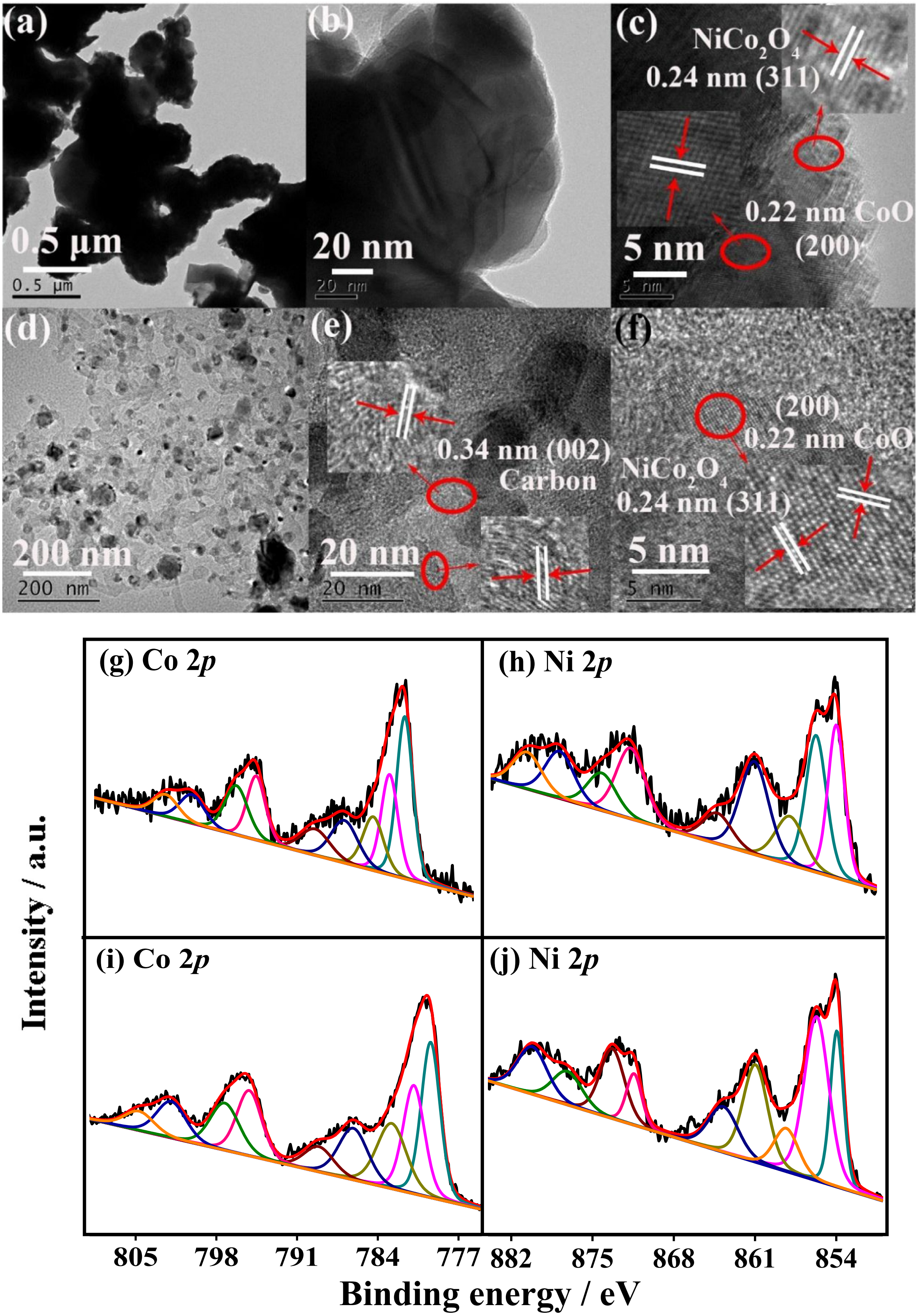

Fig. 1. TEM and HR-TEM images of (a, b, c) $NiCo_2O_4$/CoO and (d, e, f) $NiCo_2O_4$/CoO/CNTs composites. The high-resolution Co 2*p* and Ni 2*p* XPS spectra of (g, h) $NiCo_2O_4$/CoO and (i, j) $NiCo_2O_4$/CoO/CNTs composites.

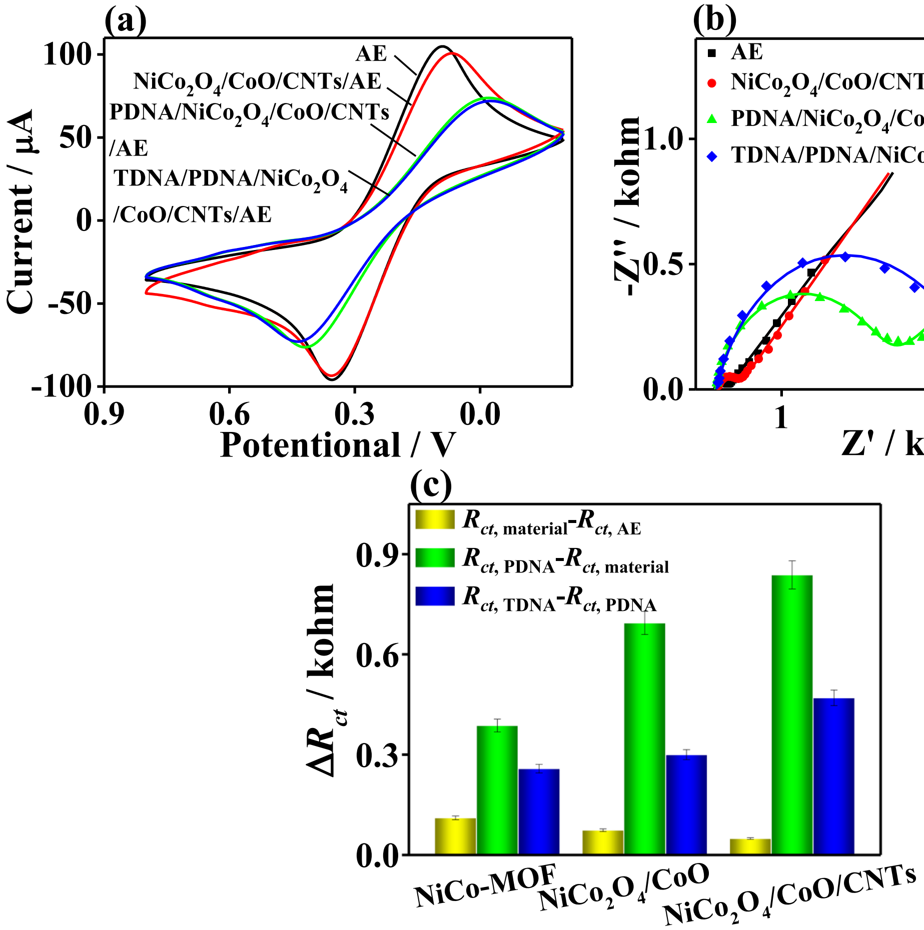

Fig. 2. (a) CV curves and (b) EIS Nyquist plots of $NiCo_2O_4$/CoO/CNTs-modified AE for detecting HIV-1 DNA, including the modification of AE with the $NiCo_2O_4$/CoO/CNTs composite, the probe DNA immobilization, and the detection of HIV-1 DNA. (c) Variations in the R_{ct} values for each stage during the fabrication procedure of different $NiCo_2O_4$/CoO/CNTs-based assays for detecting HIV-1 DNA.

(ZIF-67) under a flow of H_2/He (Aijaz et al., 2016). Xia et al. developed an in situ formation of Co-/N-doped CNTs composite from the calcination of a MOF structure (ZIF-67) under reducing atmosphere (Ar/H_2, 90%/10% volume) (Xia et al., 2016). It appears to be that there is no unconsistent statement about the formation mechanism of the carbon nanotube derived from MOFs by pyrolysis (Yu et al., 2018). In our work, CNTs was only obtained by pyrolysis under flow N_2 atmosphere. It is may be because calcination temperature, ligand, and nickel ion have a synergistic effect on the surface growth of CNTs.

3.2. Crystal and chemical structures of NiCo-MOF, $NiCo_2O_4$/CoO, and $NiCo_2O_4$/CoO/CNTs composites

The crystal and chemical structures of the NiCo-MOF, $NiCo_2O_4$/CoO, and $NiCo_2O_4$/CoO/CNTs were characterized on the basis of X-ray diffraction measurement (XRD) patterns and Raman, Fourier transform infrared spectra (FT-IR), and X-ray photoelectron spectroscopy (XPS), which were supplied in S3 in detail (See the Supplementary material). The XRD results revealed that the peaks corresponding to NiCo-MOF disappeared after high-temperature calcination. The nanocomposite derived from NiCo-MOF which was calcined under N_2 atmosphere shows the characteristic diffraction peaks of $NiCo_2O_4$ and the metallic Co, whereas the composite calcined under H_2 atmosphere exhibits CoO besides of $NiCo_2O_4$ and the metallic Co. These results indicate that the metallic coordination centers of Co and Ni were transferred into the spinel nanostructure, along with metal oxide or metallic state. The similar results were also observed for other MOFs-derivatives by calcination at high temperature (Maiti et al., 2018). Additionally, the Raman spectrum of NiCo-MOF is mainly assigned with the chemical structure of organic ligands, which is consistent with the analysis of its FT-IR spectrum. After the calcination at 700 °C under N_2 atmosphere, the $NiCo_2O_4$/CoO/CNTs shows a strong peak of CoO, along with D and G peaks, which is suggestive of the presence of C material. Combining with the results of its HR-TEM image, it hints that the organic ligands containing in NiCo-MOF were changed to CNTs during high-temperature calcination under N_2 (Zhong et al., 2017a). As for the $NiCo_2O_4$/CoO, the weak peaks corresponded to the stretching vibrations of Ni-O was observed. The metal-oxide bonds, including Co-O and Ni-O, were also obtained in the FT-IR spectra of nanocomposites, together with the absorption bands of Ni and Co present in $NiCo_2O_4$.

Moreover, the XPS spectra of all samples demonstrated that the signals of Co 2*p* (780 eV), Ni 2*p* (854 eV), C 1*s* (284 eV), N 1*s* (401 eV), and O 1*s* (529 eV) were coexisted (Fig. S4d). In order to evaluate the variation of the chemical valence states and environments of the NiCo-MOF before and after the calcination, the high-resolution XPS spectra of all elements containing in samples were analyzed by using XPSPEAK software (Figs. 1**g**-1**j**, S5, and S6) and discussed in S3 (See the Supplementary material). Figs. 1**g** and 1**i** illustrate that the different chemical valences of Co 2*p* (Co^{3+}, Co^{2+}, and Co°) and Ni 2*p* (Ni^{2+}, Ni^{3+}, and Ni°) were co-appeared in the $NiCo_2O_4$/CoO and $NiCo_2O_4$/CoO/CNTs composites. However, the metallic Co and Ni were absent from NiCo-MOF, indicating Co^{2+} and Ni^{2+} were efficiently reduced during high-temperature calcination. This transformation could affect aptamer immobilization during biosensor fabrication (Wang et al., 2018a). Three kinds of C-C, C-O, and COO groups were observed in the C 1 s XPS spectrum of the $NiCo_2O_4$/CoO composite. However, two additional weak C=O a π-π* peaks appeared in the spectrum of the $NiCo_2O_4$/CoO/CNTs composite, aside ofd C-C, C-O, and COO groups. As known, the π-π* binding originated from CNTs in the $NiCo_2O_4$/CoO/CNTs composite (Zuo et al., 2013). Furthermore, Co-O, C=O, and C-O groups were obtained from the high-resolution O 1*s* XPS of the two samples, while the peak of adsorbed O in $NiCo_2O_4$/CoO/CNTs indicates its good absorbability. The integrated analysis of all characterizations revealed that NiCo-MOF had been decomposed into various components under different atmospheres. $NiCo_2O_4$ and CoO nanoparticles were present in two composites calcined under N_2 and H_2, whereas CNTs only appeared in the composite prepared under N_2. Therefore, $NiCo_2O_4$/CoO and $NiCo_2O_4$/CoO/CNTs were selected to represent the composites calcined under H_2 and N_2 atmospheres, respectively, and were subjected to further analysis.

3.3. Electrochemical performances of all samples

Electrochemical techniques, including CV and EIS, were applied to investigate the variation in electron transfer during the development of the DNA assay based on NiCo-MOF, $NiCo_2O_4$/CoO, and $NiCo_2O_4$/CoO/CNTs. The CV curves of the $NiCo_2O_4$/CoO/CNTs-based DNA assay for the detection of HIV-1 DNA were acquired over the potential window of − 0.2–0.8 V and are shown in Fig. 2**a**. The CV curve of the bare AE showed two well-defined CV peaks that were suggestive of rapid electron transfer in the $[Fe(CN)_6]^{3-/4-}$ redox probe. The CV curve of the electrode modified with the $NiCo_2O_4$/CoO/CNTs composite was almost similar to that of the bare AE, hinting that the $NiCo_2O_4$/CoO/CNTs composite exhibited good electrochemical conductivity. It can promote electron transfer at the interface between the electrode and electrolyte and amplify electrochemical signals. The CV peak current density decreased substantially when $NiCo_2O_4$/CoO/CNTs composite was immobilized on the surfaces of the DNA probe. In aqueous solution, electron transfer would be hindered by strongly repulsive interactions with $[Fe(CN)_6]^{3-/4-}$ redox resulting from the ionization of phosphate groups in DNA strands to their negatively charged forms (Kondinskaia and Gurtovenko, 2018). When the developed assay was used to detect the HIV-1 DNA, the hybridization between the probe DNA and HIV-1 DNA slightly reduced CV peak current density (Lu et al., 2019). However, given the insufficient determination sensitivity of the CV technique, the EIS approach was also used to investigate the performance of the $NiCo_2O_4$/CoO/CNTs-based bioassay in the detection of HIV-1 DNA (Fig. 2**b**). The R_{ct} value of the bare AE electrode was only 73.13 Ω and is suggestive of excellent electrochemical conductivity. The low R_{ct} value (122 Ω) of the $NiCo_2O_4$/CoO/CNTs-modified electrode is indicative of rapid interfacial electron transfer. Herein, the formed $NiCo_2O_4$ can accelerate electron transfer given that the spinel structure exhibited better electronic conductivity and higher electrochemical activity than single Ni or Co (Liu et al., 2019). The $R_{\underline{ct}}$ value continuously increased to 0.96 kΩ when the DNA probe strand anchored onto the $NiCo_2O_4$/CoO/CNTs-modified electrode (PDNA/$NiCo_2O_4$/CoO/CNTs). As previously mentioned, the repulsive interaction between the negative charges of the phosphate groups and the $[Fe(CN)_6]^{3-/4-}$ redox hindered electron transfer, increasing the value of R_{ct}. After the detection of HIV-1 DNA, the R_{ct} value of the electrode (1.43 kΩ) further increased. The hybridization of the probe DNA and HIV-1 target DNA can impede electron transfer because of the electrochemical insulativity of oligonucleotides (Wang et al., 2018b).

For comparison, the sensing performances of NiCo-MOF and $NiCo_2O_4$/CoO in the detection of HIV-1 DNA were investigated through electrochemical methods (Fig. S7). Similar trends were observed for different bioassays. Specifically, the CV peak current densities (Figs. S7a and S7c) associated with NiCo-MOF or $NiCo_2O_4$/CoO modification, probe DNA immobilization, and HIV-1 DNA detection decreased successively. The simulated R_{ct} values for each step of detection with the developed bioassays based on various electrode materials are summarized in Table S1. The detection efficiencies of the three different assays were evaluated. The sensing performances of these assays were evaluated on the basis of the relative changes in R_{ct} values, represented as $\Delta R_{ct} = R_{ct,i+1} - R_{ct,I}$, associated with each step of HIV-1 DNA detection (Fig. 2**c**). It showed that the ΔR_{ct} value of the NiCo-MOF electrode was the largest (111 Ω), whereas those of the $NiCo_2O_4$/CoO- and $NiCo_2O_4$/CoO/CNTs- electrodes were 48.9 and 74 Ω, respectively. These findings suggest that $NiCo_2O_4$/CoO/CNTs composites demonstrated improved electrochemical activity owing to their $NiCo_2O_4$, metal oxide nanoparticle, and CNTs contents (Xu et al., 2019). The PDNA/$NiCo_2O_4$/CoO/CNTs-based assay similarly exhibited superior anchoring ability toward probe DNA and provided the largest ΔR_{ct} value (838 Ω). Moreover, the Nyquist plots obtained from the kinetics behavior of the PDNA/$NiCo_2O_4$/CoO/CNTs electrode in the electrolyte solution revealed the good stability of the probe DNA over the modified electrode (Fig. S8). After the detection of HIV-1 DNA, it showed the highest hybridization ability among the three kinds of assays as indicated by its $\triangle R_{ct}$ value of 470 Ω. Given that the $NiCo_2O_4$/CoO/CNTs composite demonstrated strong probe DNA anchoring activity and high sensitivity in HIV-1 DNA detection, it was selected as the sensitive layer for further electrochemical measurements. This composite was composed of $NiCo_2O_4$ and CoO nanoparticles that coupled with CNTs through calcination under N_2 atmosphere. The interaction between Co or Ni metallic nanoparticles and CNTs can reduce the work function and increase the number of active sites on the surfaces of CNTs by facilitating electron transfer from metallic particles to C (Hou et al., 2015; Ma et al., 2018). It can further intensify electrochemical signals and DNA anchoring on the active sites of the composite by enhancing redox activity (Chen et al., 2018a). The preferential immobilization of DNA strands onto CNTs surfaces via π-π interactions enhances sensing performance (Jiang and Lee, 2018).

3.4. Analytical performance of the $NiCo_2O_4$/CoO/CNTs-based assay

EIS measurements were performed in 0.01 M PBS containing $[Fe(CN)_6]^{3-/4-}$ to assess the sensitivity and quantitative range of the $NiCo_2O_4$/CoO/CNTs-based assay (Fig. 3**a**). The electrochemical performance of the developed assay in detecting series of HIV-1 DNA solutions with concentrations of 0.1 pM to 20 nM was monitored. The obtained ΔR_{ct} value gradually increased and approached to a level-off as the HIV-1 DNA concentration increased (Fig. 3**b**). Thus, the detection behavior of the HIV-1 DNA using the developed $NiCo_2O_4$/CoO/CNTs-based assay was obeyed to the Langmuir-Freundlich isotherm (Thapa et al., 2017). The limit of detection (LOD) using the IUPAC method:

$$\mathrm{LOD} = 3\mathrm{SD}/\mathrm{slope}$$

where SD refers to standard deviation and the slope refers to the gradient of the calibration graph. The LOD was calculated graphically from the calibration plot by considering the steep slope encompassing the first four data points (Fig. 3**b**). The LOD is calculated to be 16.7 fM.

The proposed DNA assay exhibited a lower LOD and a broader HIV-1 DNA detection range than previously reported HIV-1 DNA detection methods **(**Table 1**)**. All of these outcomes are mainly attributed to the inherent advantages of the porous $NiCo_2O_4$/CoO/CNTs composite, i.e., (i) the coexistence of CNTs, metallic nanoparticles, metal oxides, and spinel in the composite can strengthen the electrochemical response in sensing by promoting mass transfer and provide conductive paths to accelerate the charge transport necessary for electrochemical reactions; (ii) the metal oxide core(CoO and $NiCo_2O_4$) and CNTs can facilitate the binding of the probe DNA strands through the integrated interaction of hydrogen bonds, π-π* interaction, and electrostatic force (Zhou and Pang, 2018); (iii) the retention of the inherent cavities of NiCo-MOF by the composites enabled probe DNA strands to adsorb over the composite surface and to penetrate the composite interior, thus improving the sensing performances of the HIV-1 target DNA (Wang et al., 2018c); and (iv) the good biocompatibility of the composite promotes the stabilization of the hybridized double DNA strands.

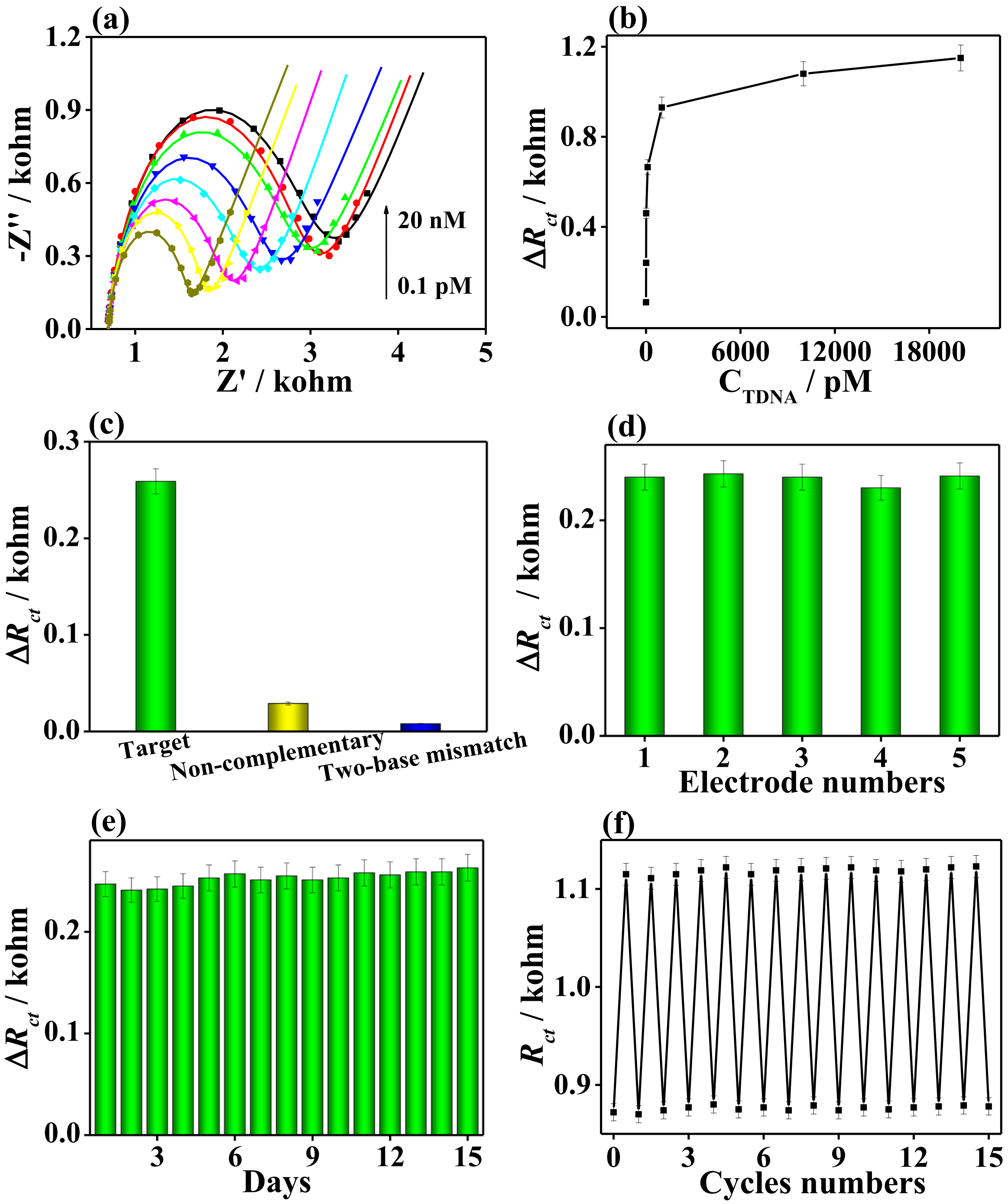

Fig. 3. (c) EIS Nyquist plots for the detection of different concentrations of HIV-1 DNA (0.1, 1, 10, 100, 1000, 10,000 and 20,000 pM) using the $NiCo_2O_4$/CoO/CNTs-based assay; (d) the corresponding calibration curves between ΔR_{ct} and HIV-1 DNA concentrations (Inset: the linear fit plot of ΔR_{ct} as function of the logarithm of the HIV − 1 DNA concentration (n = 3)). (e) Selectivity and (f) reproducibility of the $NiCo_2O_4$/CoO/CNTs-based assay for detecting 1.0 p.M. HIV − 1 DNA (n = 3).

Table 1
Comparison with other reported techniques for the HIV-1 gene detection.

Materials	Techniques	Linear range	LODs	Refs
AuNPs quencher	Fluorescence resonance energy transfer	50 fM-1 nM	15 fM	(Qaddare and Salimi, 2017)
AgNCs@Carbon nanoparticles oxide	Fluorescence	1–50 nM	400 pM	(Ye et al., 2016)
DNA	Colorimetric Assay	0.5 pM-1 nM	0.5 pM	(Wang et al., 2017)
Graphene-Nafion composites	Impedimetric	100 fM-100 pM	23 fM	(Gong et al., 2017)
EuS nanocrystal	Electrochemiluminesence	3 fM-0.3 nM	0.3 fM	(Babamiri et al., 2018)
hpDNA-based	Amperometry	10 pM-50 nM	18 pM	(Gao et al., 2018)
$NiCo_2O_4$/CoO/CNTs	**EIS**	**0.1 pM-20 nM**	**16.7 fM**	**This work**

3.5. Selectivity measurements

The specificity of the $NiCo_2O_4$/CoO/CNTs-based assay for complementary target HIV-1 DNA was evaluated through EIS (Fig. S9) and on the basis of the ΔR_{ct} ($\Delta R_{ct} = R_{ct,i+1} - R_{ct,i}$) values obtained for various PBS solutions (pH 7.4, 0.01 M) containing two-base mismatched DNA, noncomplementary DNA, and $[Fe(CN)_6]^{3-/4-}$ (Fig. 3**c**). The resulting ΔR_{ct} values obtained by the $NiCo_2O_4$/CoO/CNTs-based assay in the detection of complementary, mismatched, and noncomplementary DNA strands were 259, 29, and 8 Ω, respectively. These results showed that the response of the $NiCo_2O_4$/CoO/CNTs-based assay to the two-base mismatch sequence was approximately 11.2% of that for the complementary sequence because the mismatch sequence was highly structurally similar to the complementary sequence (Chen et al., 2018b). This result indicated that the $NiCo_2O_4$/CoO/CNTs-based assay can distinguish between two-base mismatch DNA and noncomplementary DNA strands and suggested that the sensor has high specificity for the fully complementary target.

The reproducibility and stability of the $NiCo_2O_4$/CoO/CNTs-based assay were also investigated through the EIS approach. As shown in Fig. 3**d**, the EIS measurements of five same $NiCo_2O_4$/CoO/CNTs-modified electrodes were acquired to assess the long-term performance of the assay. The calculated ΔR_{ct} values remained almost constant with a low relative standard deviation of 4.31% ($n = 3$). In addition, the storage stability of the $NiCo_2O_4$/CoO/CNTs-based assay was evaluated by storing the electrode at 4 °C. Storage stability was continuously measured every day for 15 days (Fig. 3**e**). The final electrochemical EIS response of the as-developed $NiCo_2O_4$/CoO/CNTs-based assay was maintained stable. All of these results suggested that the $NiCo_2O_4$/CoO/CNTs-based assay exhibited excellent reproducibility and stability. Additionally, the regenerability of the fabricated $NiCo_2O_4$/CoO/CNTs-based assay was evaluated. The TDNA/PDNA/$NiCo_2O_4$/CoO/CNTs electrode was immersed in 1.0 M NaOH at 4 °C for 10 min, washed with ultrapure water. As such, the bioassay was regenerated and then used to detect the HIV-1 DNA again (0.1 pg mL^{-1}). The operation was repeated after the detection response of the assay reached the original level. Fig. 3**h** shows the R_{ct} values of the assay for 15 regeneration runs. The slight reduction in R_{ct} value indicates that the $NiCo_2O_4$/CoO/CNTs-based assay can be facilely regenerated.

3.6. Real sample analysis

Recovery experiments with real samples were performed to investigate the practical applications of the proposed biosensor. The HIV-1 DNA target was added at different concentrations (i.e., 0.1, 1, 10, 100, 1000, and 10,000 pM) to healthy human serum samples diluted by 200-fold with PBS (0.01 M, pH 7.4). The samples were detected trice. As shown in Table S2, the proposed biosensor exhibited good sensitivity and a high recovery percentage in real human serum samples. The recoveries and relative standard deviation values were in the range of 101.85–111.94% and 2.9–4.4%, respectively. Thus, the proposed biosensor offers a reliable method for the determination of HIV-1 DNA in biologically relevant matrixes.

4. Conclusion

A bimetallic NiCo-MOF was synthesized and then calcined at 700 °C under N_2 and H_2 atmosphere to develop novel nanocomposites. Coordinated metal ion centers were transferred to Ni Co spinel, Co oxide, and metallic Co/Ni, whereas organic ligands were changed into intertwined CNTs (represented by $NiCo_2O_4$/CoO@CNTs) at 700 °C under N_2 atmosphere. Synergism among the different components of the $NiCo_2O_4$/CoO@CNTs nanocomposite resulted in the excellent electrochemical activity, good biocompatibility, and strong bioaffinity of the probe DNA. The feasibility of using the $NiCo_2O_4$/CoO@CNTs composite as the probe DNA scaffold for the detection of HIV-1 DNA was explored, which was superior to the pristine NiCo-MOF and $NiCo_2O_4$/CoO obtained from the calcination of NiCo-MOF under H_2 atmosphere. The $NiCo_2O_4$/CoO@CNTs-based bioassay displayed an ultralow detection limit of 16.7 fM for the HIV-1 DNA over the wide linear range of 0.1 pM to 20 nM. It also demonstrated good selectivity even against noncomplementary and two-base mismatch DNA sequences and showed high stability, reproducibility, and stability. The developed $NiCo_2O_4$/CoO@CNTs-based bioassay also can be easily regenerated by using NaOH solution and was successfully applied to detect HIV-1 DNA in human serum samples. The proposed method represents an alternative approach for the detection of HIV-1 genes at trace amounts and extends the sensing applications of MOFs.

CRediT authorship contribution statement

Zhankui Jia: Validation, Formal analysis. **Yashen Ma:** Writing - original draft. **Longyu Yang:** Formal analysis, Investigation. **Chuanpan Guo:** Methodology, Formal analysis. **Nan Zhou:** Conceptualization, Writing - review & editing, Supervision. **Linghao He:** Writing - review & editing. **Zhihong Zhang:** Writing - review & editing, Supervision.

Acknowledgements

This work was supported by Programs for the National Natural Science Foundation of China (NSFC: Account No. U1604127).

Declaration of interest statement

We declare that we have no conflict of interest.

Appendix A. Supporting information

Supplementary data associated with this article can be found in the online version at doi:10.1016/j.bios.2019.03.030.

References

Aijaz, A., Masa, J., Rösler, C., Xia, W., Weide, P., Botz, A.J.R., Fischer, R.A., Schuhmann, W., Muhler, M., 2016. Angew. Chem. Int. Ed. 55, 4087–4091.

Ali, Z., Wang, J., Tang, Y., Liu, B., He, N., Li, Z., 2017. Biomater. Sci. 5, 57–66.

Ambinder, R.F., Bhatia, K., Martinez-Maza, O., Mitsuyasu, R., 2010. Curr. Opin. HIV AIDS 5, 531–537.

Babamiri, B., Salimi, A., Hallaj, R., 2018. Biosens. Bioelectron. 117, 332–339.

Carinelli, S., Xufré Ballesteros, C., Martí, M., Alegret, S., Pividori, M.I., 2015. Biosens. Bioelectron. 74, 974–980.

Chen, L., Zheng, H., Zhu, X., Lin, Z., Guo, L., Qiu, B., Chen, G., Chen, Z., 2013. Analyst 138, 3490–3493.

Chen, Y., Guo, S., Zhao, M., Zhang, P., Xin, Z., Tao, J., Bai, L., 2018a. Biosens. Bioelectron. 119, 215–220.

Chen, Y., Kuo, W., Tai, T., Hsu, C., Sarangadharan, I., Pulikkathodi, A.K., Wang, S., Sukesan, R., Lin, H., Kao, K., Hsu, C., Chen, C., Wang, Y., 2018b. Sens. Actuator B-Chem. 262, 365–370.

Du, M., Chen, M., Yang, X., Wen, J., Wang, X., Fang, S., Liu, C., 2014. J. Mater. Chem. A 2, 9828–9834.

Gao, X., Wang, X., Li, Y., He, J., Yu, H., 2018. Anal. Chem. 90, 8147–8153.

Gong, Q., Wang, Y., Yang, H., 2017. Biosens. Bioelectron. 89, 565–569.

Guo, C., Su, F., Song, Y., Hu, B., Wang, M., He, L., Peng, D., Zhang, Z., 2017. ACS Appl. Mater. Inter. 9, 41188–41199.

He, L., Duan, F., Song, Y., Guo, C., Zhao, H., Tian, J., Zhang, Z., Liu, C., Zhang, X., Wang, P., Du, M., Fang, S., 2017. 2D Mater. 4, 25098.

Hou, Y., Cui, S., Wen, Z., Guo, X., Feng, X., Chen, J., 2015. Small 11, 5940–5948.

Huo, R., Jiang, W., Xu, S., Zhang, F., Hu, J., 2014. Nanoscale 6, 203–206.

Jiang, H., Lee, E., 2018. Biosens. Bioelectron. 118, 16–22.

Jin, J., Zheng, Y., Huang, S., Sun, P., Srikanth, N., Kong, L.B., Yan, Q., Zhou, K., 2019. J. Mater. Chem. A 7, 783–790.

Kondinskaia, D.A., Gurtovenko, A.A., 2018. Polymer 142, 277–284.

Li, W., Lv, S., Wang, Y., Zhang, L., Cui, X., 2019. Sens. Actuator B-Chem. 281, 652–658.

Lillis, L., Lehman, D.A., Siverson, J.B., Weis, J., Cantera, J., Parker, M., Piepenburg, O., Overbaugh, J., Boyle, D.S., 2016. J. Virol. Methods 230, 28–35.

Liu, J., Hou, M., Yi, J., Guo, S., Wang, C., Xia, Y., 2014. Energ. Environ. Sci. 7, 705–714.

Liu, Y., Liu, P., Qin, W., Wu, X., Yang, G., 2019. Electrochim. Acta 297, 623–632.

Lu, L., Wang, J., Miao, W., Wang, X., Guo, G., 2019. Anal. Chem. 91, 1452–1459.

Ma, L., Wang, R., Li, Y., Liu, X., Zhang, Q., Dong, X., Zang, S., 2018. J. Mater. Chem. A 6,

24071–24077.
Maiti, S., Pramanik, A., Dhawa, T., Sreemany, M., Mahanty, S., 2018. Mat. Sci. Eng. B 229, 27–36.
Otange, B.O., Birech, Z., Okonda, J., Rop, R., 2017. Anal. Bioanal. Chem. 409, 3253–3259.
Pan, Y., Zhan, S., Xia, F., 2018. Anal. Biochem. 546, 5–9.
Peng, B., Cui, J., Wang, Y., Liu, J., Zheng, H., Jin, L., Zhang, X., Zhang, Y., Wu, Y., 2018. Nanoscale 10, 1939–1945.
Qaddare, S.H., Salimi, A., 2017. Biosens. Bioelectron. 89, 773–780.
Rackus, D.G., Shamsi, M.H., Wheeler, A.R., 2015. Chem. Soc. Rev. 44, 5320–5340.
Rezaee, S., Shahrokhian, S., 2019. Appl. Catal. B-Environ. 244, 802–813.
Shu, Y., Yan, Y., Chen, J., Xu, Q., Pang, H., Hu, X., 2017. ACS Appl. Mater. Inter. 9, 22342–22349.
Thapa, A., Soares, A.C., Soares, J.C., Awan, I.T., Volpati, D., Melendez, M.E., Fregnani, J.H.T.G., Carvalho, A.L., Oliveira, O.N., 2017. ACS Appl. Mater. Inter. 9, 25878–25886.
Wang, M., Yang, L., Hu, B., Liu, J., He, L., Jia, Q., Song, Y., Zhang, Z., 2018b. Biosens. Bioelectron. 113, 16–24.
Wang, H., Ma, R., Sun, F., Jia, L., Zhang, W., Shang, L., Xue, Q., Jia, W., Wang, H., 2018b. Biosens. Bioelectron. 122, 224–230.
Wang, M., Hu, B., Yang, C., Zhang, Z., He, L., Fang, S., Qu, X., Zhang, Q., 2018a. Biosens. Bioelectron. 99, 176–185.
Wang, K., Fan, D., Liu, Y., Dong, S., 2017. Biosens. Bioelectron. 87, 116–121.
Wang, S., Li, Z., Duan, F., Hu, B., He, L., Wang, M., Zhou, N., Jia, Q., Zhang, Z., 2019. Anal. Chim. Acta 1047, 150–162.
Wang, Y., Shi, R., Lin, J., Zhu, Y., 2011. Energ. Environ. Sci. 4, 2922–2929.
Wu, S., Liu, J., Cui, B., Li, Y., Liu, Y., Hu, B., He, L., Wang, M., Zhang, Z., Tian, K., Song, Y., 2019. Electrochim. Acta 299, 231–244.
Xia, B.Y., Yan, Y., Li, N., Wu, H.B., Lou, X.W.D., Wang, X., 2016. Nat. Energy 1, 15006.
Xu, Y., Yan, Y., He, T., Zhan, K., Yang, J., Zhao, B., Qi, K., Xia, B.Y., 2019. Carbon 145, 201–208.
Ye, Y., Xia, L., Xu, D., Xing, X., Pang, D., Tang, H., 2016. Biosens. Bioelectron. 85, 837–843.
Yu, Z., Bai, Y., Zhang, S., Liu, Y., Zhang, N., Wang, G., Wei, J., Wu, Q., Sun, K., 2018. ACS Appl. Mater. Inter. 10, 6245–6252.
Zhang, Z., Ji, H., Song, Y., Zhang, S., Wang, M., Jia, C., Tian, J., He, L., Zhang, X., Liu, C., 2017. Biosens. Bioelectron. 94, 358–364.
Zhao, S., Wang, Y., Dong, J., He, C., Yin, H., An, P., Zhao, K., Zhang, X., Gao, C., Zhang, L., Lv, J., Wang, J., Zhang, J., Khattak, A.M., Khan, N.A., Wei, Z., Zhang, J., Liu, S., Zhao, H., Tang, Z., 2016. Nat. Energy 1, 16184.
Zhao, W., Han, Y., Zhu, Y., Zhang, N., Xu, J., Chen, H., 2015. Anal. Chem. 87, 5496–5499.
Zhong, H., Luo, Y., He, S., Tang, P., Li, D., Alonso-Vante, N., Feng, Y., 2017a. ACS Appl. Mater. Interfaces 9, 2541–2549.
Zhong, H., Luo, Y., He, S., Tang, P., Li, D., Alonso-Vante, N., Feng, Y., 2017b. ACS Appl. Mater. Interfaces 9, 2541–2549.
Zhou, H., Pang, X., 2018. Chem. Rev. 118, 1691–1741.
Zhou, L., Huang, J., Yu, B., Liu, Y., You, T., 2015. ACS Appl. Mater. Inter. 7, 24438–24445.
Zhou, N., Su, F., Guo, C., He, L., Jia, Z., Wang, M., Jia, Q., Zhang, Z., Lu, S., 2019. Biosens. Bioelectron. 123, 51–58.
Zhu, Q., Xu, Q., 2014. Chem. Soc. Rev. 43, 5468–5512.
Zuo, G., Kang, S., Xiu, P., Zhao, Y., Zhou, R., 2013. Small 9, 1546–1556.